

# Compatibility and Interaction Mechanism between the C<sub>4</sub>F<sub>7</sub>N/CO<sub>2</sub>/O<sub>2</sub> Gas Mixture and FKM and NBR

Ran Zhuo, Junyi Chen, Song Xiao, Mingli Fu,\* Dibo Wang, Xiangyu Tan,\* Yi Li, Peng Wu, Ju Tang, and Xiaoxing Zhang



Cite This: *ACS Omega* 2023, 8, 11414–11424



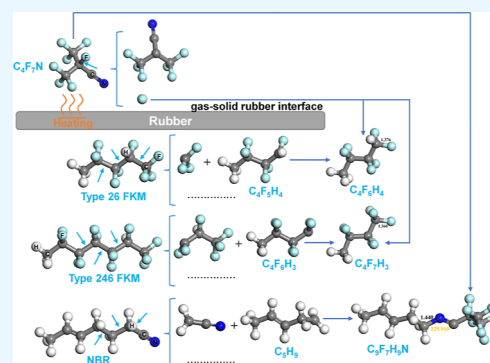
Read Online

ACCESS |

Metrics & More

Article Recommendations

**ABSTRACT:** The C<sub>4</sub>F<sub>7</sub>N/CO<sub>2</sub>/O<sub>2</sub> gas mixture received a great deal of attention for its potential use in eco-friendly gas-insulated equipment (GIE). The evaluation of the compatibility between C<sub>4</sub>F<sub>7</sub>N/CO<sub>2</sub>/O<sub>2</sub> and sealing rubber is necessary and significant considering the high working pressure (0.14–0.6 MPa) of GIE. Herein, we explored the compatibility between C<sub>4</sub>F<sub>7</sub>N/CO<sub>2</sub>/O<sub>2</sub> and fluororubber (FKM) and nitrile butadiene rubber (NBR) for the first time by analyzing the gas components, rubber morphology, elemental composition, and mechanical properties. The interaction mechanism of the gas–rubber interface was further investigated based on the density functional theory. We found that C<sub>4</sub>F<sub>7</sub>N/CO<sub>2</sub>/O<sub>2</sub> is compatible with FKM and NBR at 85 °C, while the surface morphology changed at 100 °C, with white granular and agglomerated lumps appearing on FKM and multi-layer flakes being generated on NBR. The accumulation of the fluorine element occurred, and the compressive mechanical properties of NBR deteriorated after the gas–solid rubber interaction. Overall, the compatibility between FKM and C<sub>4</sub>F<sub>7</sub>N/CO<sub>2</sub>/O<sub>2</sub> is superior, which could be employed as the sealing material for C<sub>4</sub>F<sub>7</sub>N-based GIE.



## 1. INTRODUCTION

In recent years, fluorinated nitrile (C<sub>4</sub>F<sub>7</sub>N) has been considered to be the most potential alternative gas for sulfur hexafluoride (SF<sub>6</sub>) employed in gas-insulated equipment (GIE).<sup>1–3</sup> Its dielectric strength reaches twice that of SF<sub>6</sub>, with a global warming potential of 2090. For engineering applications, CO<sub>2</sub> is mostly mixed with C<sub>4</sub>F<sub>7</sub>N to meet the minimum operating temperature requirements of GIE.<sup>4</sup> In addition, O<sub>2</sub> is selected as the regulatory gas to inhibit the formation of solid by-products.<sup>5</sup> At present, explorations on the basic insulation performance of the C<sub>4</sub>F<sub>7</sub>N/CO<sub>2</sub>/O<sub>2</sub> gas mixture have confirmed its application feasibility; equipment manufacturers such as General Electric have also introduced eco-friendly GIE, with C<sub>4</sub>F<sub>7</sub>N/CO<sub>2</sub>/O<sub>2</sub> as the insulating medium.

Mostly, the operating gas pressure of GIE is at 0.14–0.6 MPa. Considering the insulating properties of C<sub>4</sub>F<sub>7</sub>N/CO<sub>2</sub>/O<sub>2</sub> are closely related to gas pressure, the sealing material is required to work reliably to ensure operational safety. At present, GIE mostly uses O-ring rubber such as an ethylene propylene diene monomer (EPDM), nitrile butadiene rubber (NBR), fluororubber (FKM), a fluorosilicone elastomer, and alkyl ester acrylate as sealing materials.<sup>6</sup> First, the sealing ring is in close contact with the gas-insulating medium during long-term operation and is subjected to a combination of electrical, thermal, and mechanical stresses. Moreover, the operation and

maintenance period of GIE generally reaches more than 6 months. Therefore, it is necessary to systematically evaluate the compatibility between C<sub>4</sub>F<sub>7</sub>N/CO<sub>2</sub>/O<sub>2</sub> and rubber sealing materials before large-scale engineering applications to avoid the sealing failure induced by the gas–solid rubber interface reactions.<sup>7,8</sup>

Currently, explorations on the compatibility between C<sub>4</sub>F<sub>7</sub>N and rubber materials have made some achievements. Kessler et al. found that there existed a strong interaction between the rubber, desiccant, and C<sub>4</sub>F<sub>7</sub>N, leading to the formation of C<sub>3</sub>F<sub>7</sub>H and C<sub>3</sub>F<sub>6</sub>.<sup>9</sup> Zhang et al. analyzed the compatibility between EPDM and C<sub>4</sub>F<sub>7</sub>N/CO<sub>2</sub> and found that the gas–solid interaction produced C<sub>3</sub>F<sub>6</sub>, CF<sub>3</sub>H, and C<sub>2</sub>F<sub>5</sub>H at 80 °C (90 h), with granular crystals deposited on the EPDM.<sup>10</sup> Zhou et al. further pointed out that the gas–solid interaction resulted in significant deterioration of the mechanical properties of EPDM and the precipitation of multi-layered cross-sectional cracks with sulfite crystals.<sup>11</sup> Existing studies confirm that EPDM has poor compatibility with the C<sub>4</sub>F<sub>7</sub>N gas mixture, and further

Received: January 11, 2023

Accepted: March 2, 2023

Published: March 15, 2023



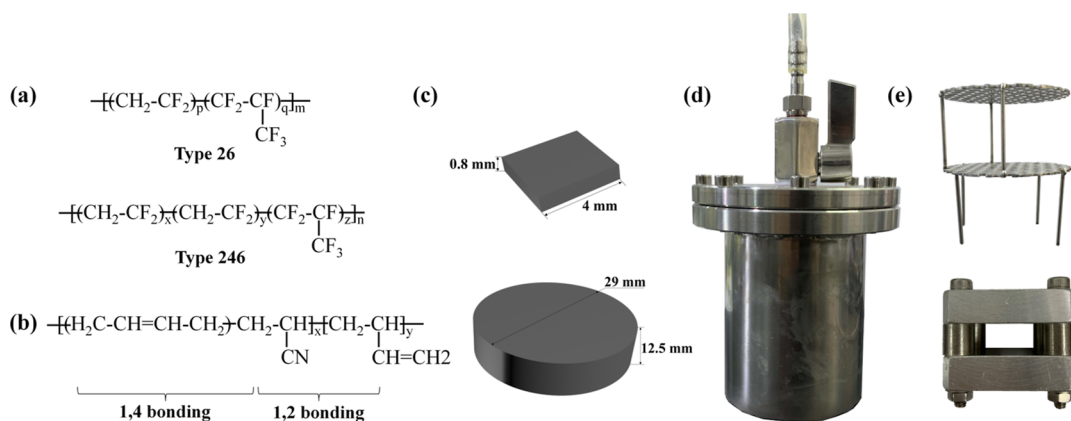


**Figure 1.** (a) Molecular structure of FKM. (b) Molecular structure of NBR. (c) Stainless-steel chamber for accelerated thermal aging tests. (d) Dimension illustration of the rubber sample. (e) Images of the double-layer stainless steel-perforated disc and fixture.

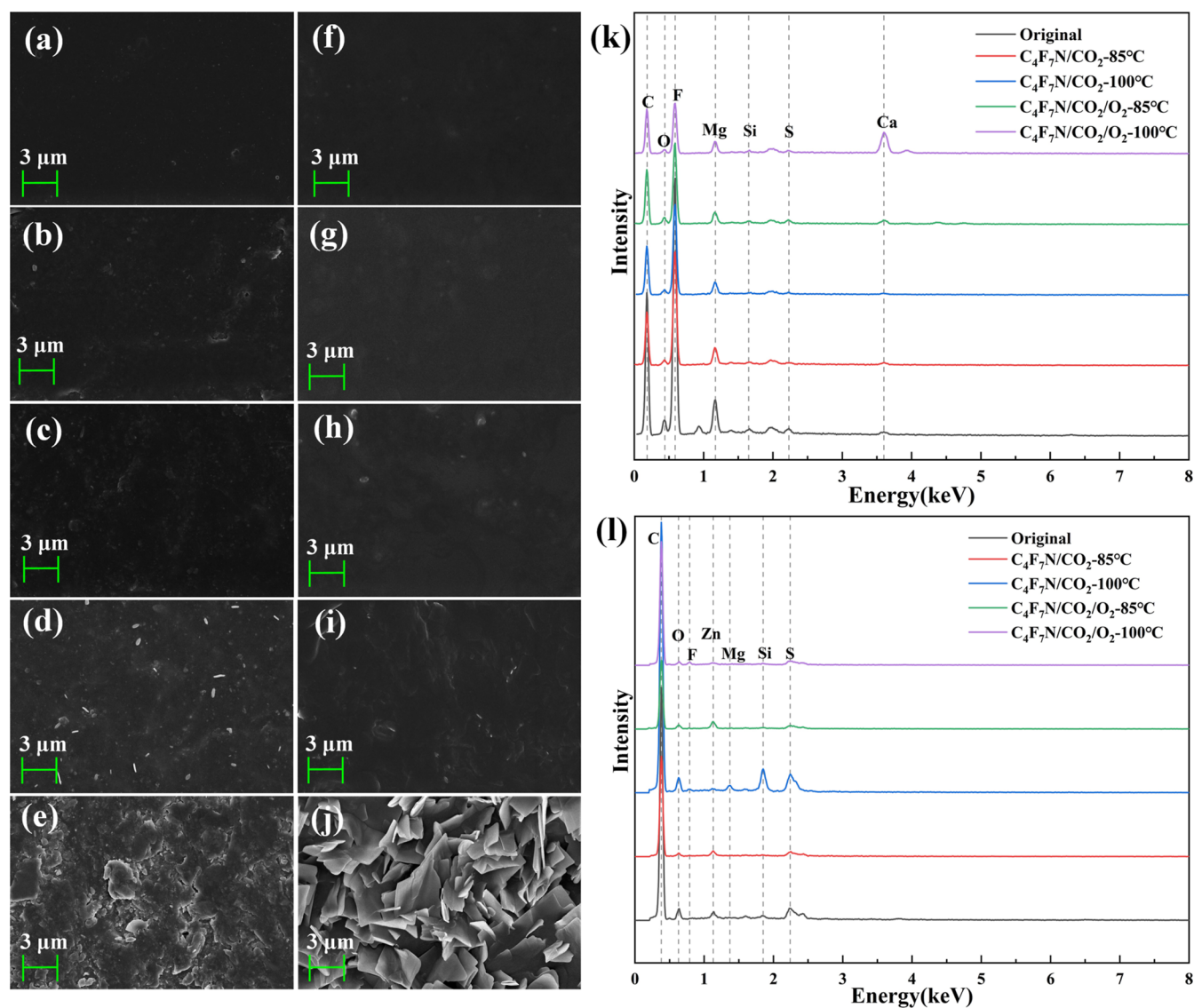


**Figure 2.** Morphology and element composition of the rubber sample before and after the interaction. (a) Untreated FKM. (b) FKM- $\text{C}_4\text{F}_7\text{N}/\text{CO}_2\text{-}85^\circ\text{C}$ . (c) FKM- $\text{C}_4\text{F}_7\text{N}/\text{CO}_2/\text{O}_2\text{-}85^\circ\text{C}$ . (d) FKM- $\text{C}_4\text{F}_7\text{N}/\text{CO}_2\text{-}100^\circ\text{C}$ . (e) FKM- $\text{C}_4\text{F}_7\text{N}/\text{CO}_2/\text{O}_2\text{-}100^\circ\text{C}$ . (f) Untreated NBR. (g) NBR- $\text{C}_4\text{F}_7\text{N}/\text{CO}_2\text{-}85^\circ\text{C}$ . (h) NBR- $\text{C}_4\text{F}_7\text{N}/\text{CO}_2/\text{O}_2\text{-}85^\circ\text{C}$ . (i) NBR- $\text{C}_4\text{F}_7\text{N}/\text{CO}_2\text{-}100^\circ\text{C}$ . (j) NBR- $\text{C}_4\text{F}_7\text{N}/\text{CO}_2/\text{O}_2\text{-}100^\circ\text{C}$ . (k) Energy spectrum of the FKM surface. (l) Energy spectrum of the NBR surface.

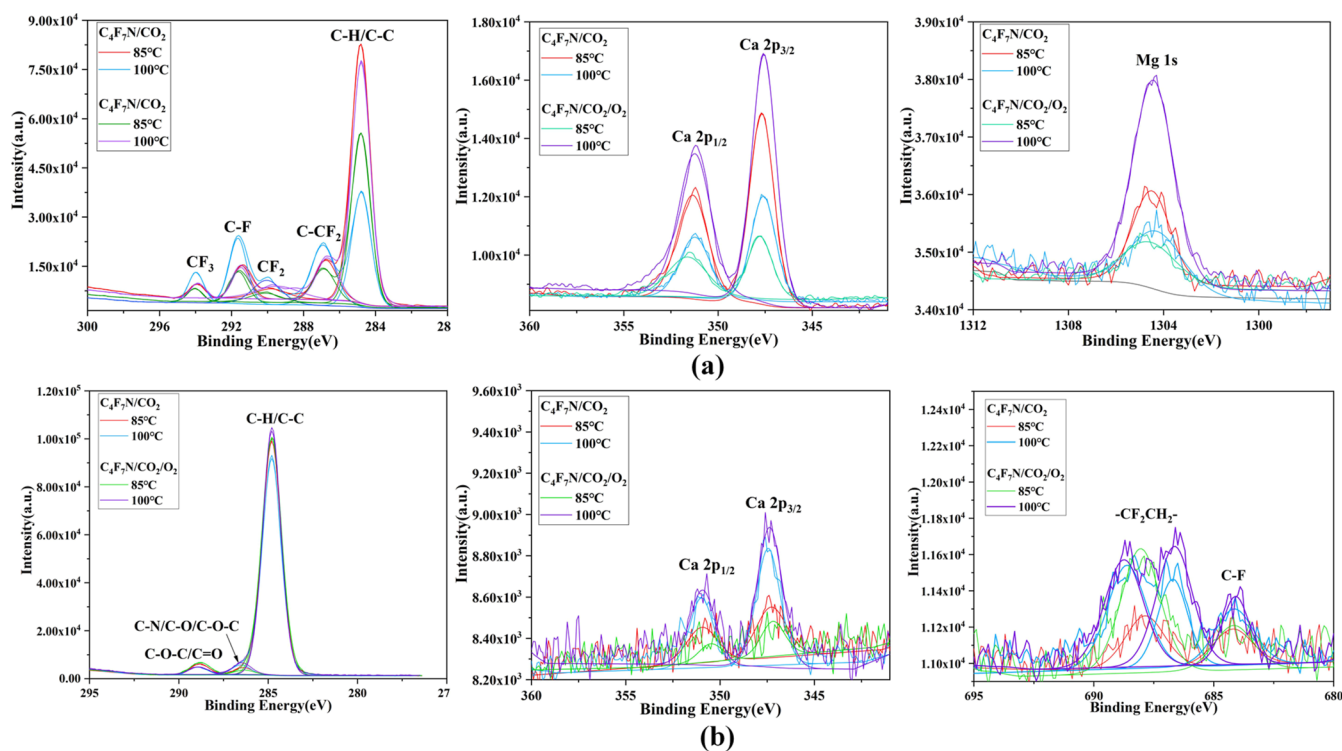


**Figure 3.** (a) XPS spectra for the surface of FKM. (b) XPS spectra for the surface of NBR.

investigations on the compatibility as well as the interaction mechanism between sealing materials and the C<sub>4</sub>F<sub>7</sub>N gas mixture are necessary.

FKM is a family of sealing materials containing fluorocarbon groups, which demonstrates great resistance to heat, oxidation, and corrosion owing to the shielding effect of C–F bonds.<sup>12</sup> Among them, the polymeric monomers of type 26 and type 246 FKM with a fluorine content of 66 and 68% are usually used in electrical engineering. In addition, NBR formed by the polymerization of butadiene and acrylonitrile also has superior heat- and oil-resistance performance.<sup>13</sup> Herein, we presented the accelerated thermal aging tests for FKM, NBR, and C<sub>4</sub>F<sub>7</sub>N/CO<sub>2</sub> and C<sub>4</sub>F<sub>7</sub>N/CO<sub>2</sub>/O<sub>2</sub> gas mixtures to reveal the compatibility between them. A systematic analysis of the characteristic parameters was carried out to reveal the gas composition, rubber morphology, elemental composition, as well as mechanical properties. Furthermore, the microscopic gas–solid interaction mechanism between FKM and NBR and C<sub>4</sub>F<sub>7</sub>N gas was analyzed based on the density functional theory (DFT). Relevant results will provide a basis for the selection of sealing materials for C<sub>4</sub>F<sub>7</sub>N/CO<sub>2</sub>/O<sub>2</sub>-based GIE.

## 2. METHODS

**2.1. Materials.** The FKM and NBR used in this paper are from Pinggao Group Co., Ltd. The degree of cross-linking of FKM and NBR is 23–28%. The type 26 and type 246-mixed FKM with the molecular formulas shown in Figure 1a were selected. In detail, type 26 FKM is a copolymer of vinylidene fluoride and hexafluoropropylene. Type 246 FKM is a copolymer of vinylidene fluoride, tetrafluoroethylene, and hexafluoropropylene. The fluorine content of the two types of FKM is 66 and 68%, respectively. Type 26 FKM has superior mechanical properties and excellent airtightness, and the reduction of hydrogen atoms brings outstanding heat resistance to type 246 FKM.<sup>14</sup> The mass ratio of 26 and 246

FKM in the mixed FKM is 50:50. The molecular chain of NBR is composed of butadiene and acrylonitrile, in which butadiene is mainly bonded with a 1,4 structure and a small part is bonded with a 1,2 structure (Figure 1b).

The rubber samples for accelerated thermal aging tests were cut into square sheets (side length: 4 mm, thickness: 0.8 mm) for morphological and elemental characterization or cylindrical specimens (diameter: 29 mm, thickness: 12.5 mm) for the mechanical property test (compressive modulus and permanent compression deformation), as shown in Figure 1c. The dimension parameters of samples were selected according to the standard ISO 815-1:2019. C<sub>4</sub>F<sub>7</sub>N (purity > 99.2%) and CO<sub>2</sub> (purity > 99.999%) were supplied by 3M China and Wuhan Neurod Special Gas Company, respectively.

**2.2. Experimental Methods.** The schematic diagram of the gas–solid rubber compatibility device is given in Figure 1d,e. The stainless-steel chamber with the volume of 0.3 L could withstand the high pressure of 0.6 MPa. The double-layer stainless steel-perforated disc set in the center of the chamber was used to place the rubber samples. The fixture clearance for permanent compression deformation was set to 9.375 mm to ensure the 25% compression of the cylindrical rubber sample during the test. Considering the minimum operating temperature of 15% C<sub>4</sub>F<sub>7</sub>N/85% CO<sub>2</sub> reaches –25 °C at 0.14 MPa and the optimal 6% O<sub>2</sub> is recommended for engineering application,<sup>15–17</sup> the 15% C<sub>4</sub>F<sub>7</sub>N/85% CO<sub>2</sub> and 15% C<sub>4</sub>F<sub>7</sub>N/79% CO<sub>2</sub>/6% O<sub>2</sub> gas mixtures were selected to conduct the gas–solid rubber compatibility tests. The aging temperatures of 85 and 100 °C were chosen, the accelerated thermal aging period was 28 days according to the ISO 23529:2016 standard, and the experimental pressure was set to 0.3 MPa to accelerate the aging process.

The chamber with rubber samples was cleaned with pure CO<sub>2</sub> three times after vacuuming to avoid the influence of impurity gases. Then, the C<sub>4</sub>F<sub>7</sub>N/CO<sub>2</sub> and C<sub>4</sub>F<sub>7</sub>N/CO<sub>2</sub>/O<sub>2</sub>

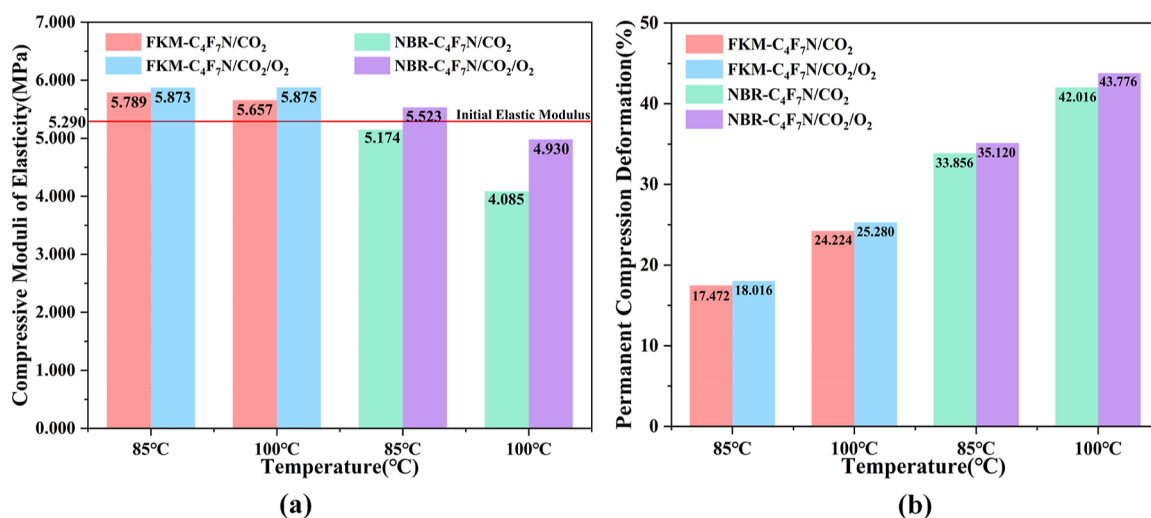


**Figure 4.** Parameters of compressive mechanical properties before and after the experiment. (a) Compressive modulus of elasticity. (b) Permanent compression deformation.

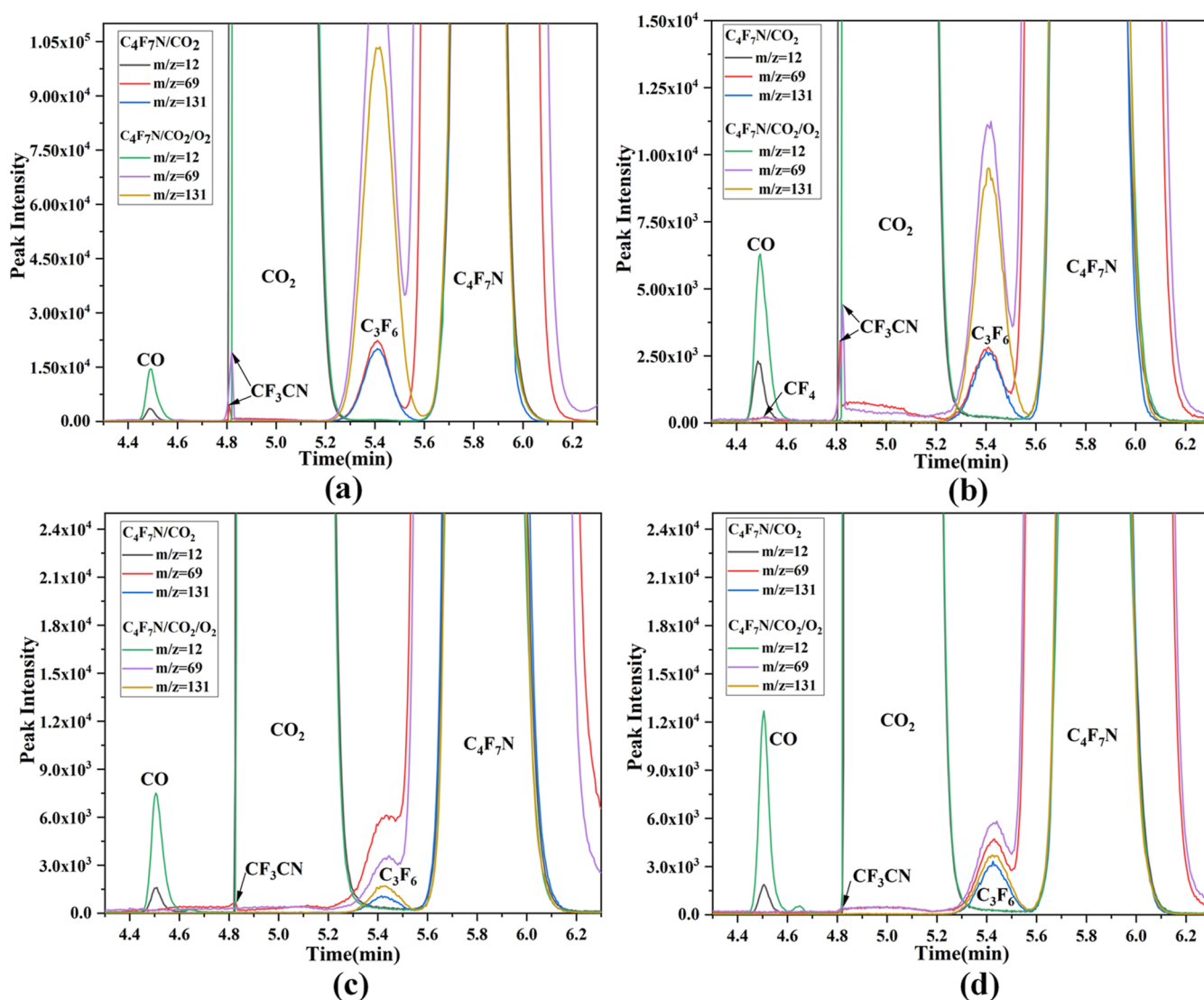


**Figure 5.** Gas component diagram. (a) FKM-85 °C; (b) FKM-100 °C. (c) NBR-85 °C. (d) NBR-100 °C.

gas mixtures were filled, and the chambers were placed in an incubator for 28 days to experience the accelerated thermal

aging tests. Gas chromatography–mass spectrometry (GC–MS) (Shimadzu Ultra 2010plus with a CP-Sil 5 CB column)

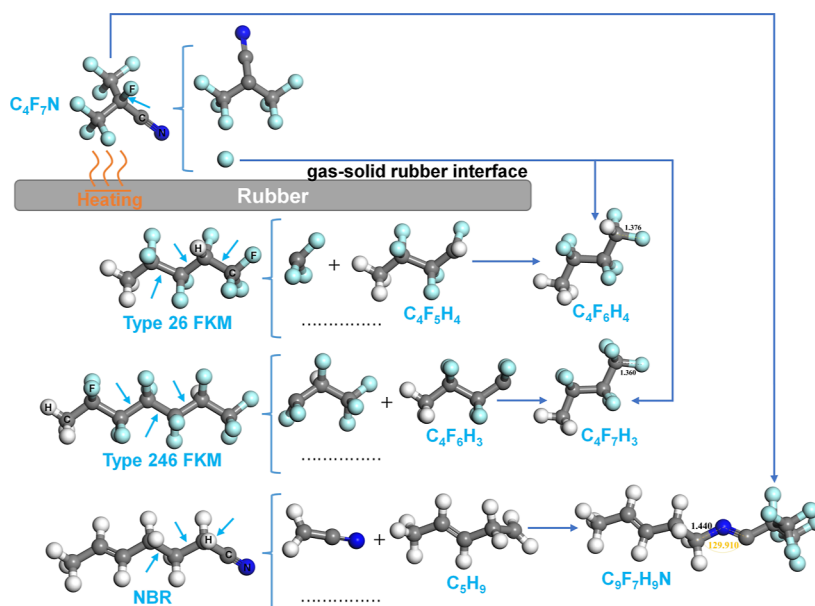


Figure 6. Gas–solid rubber interface reactions.

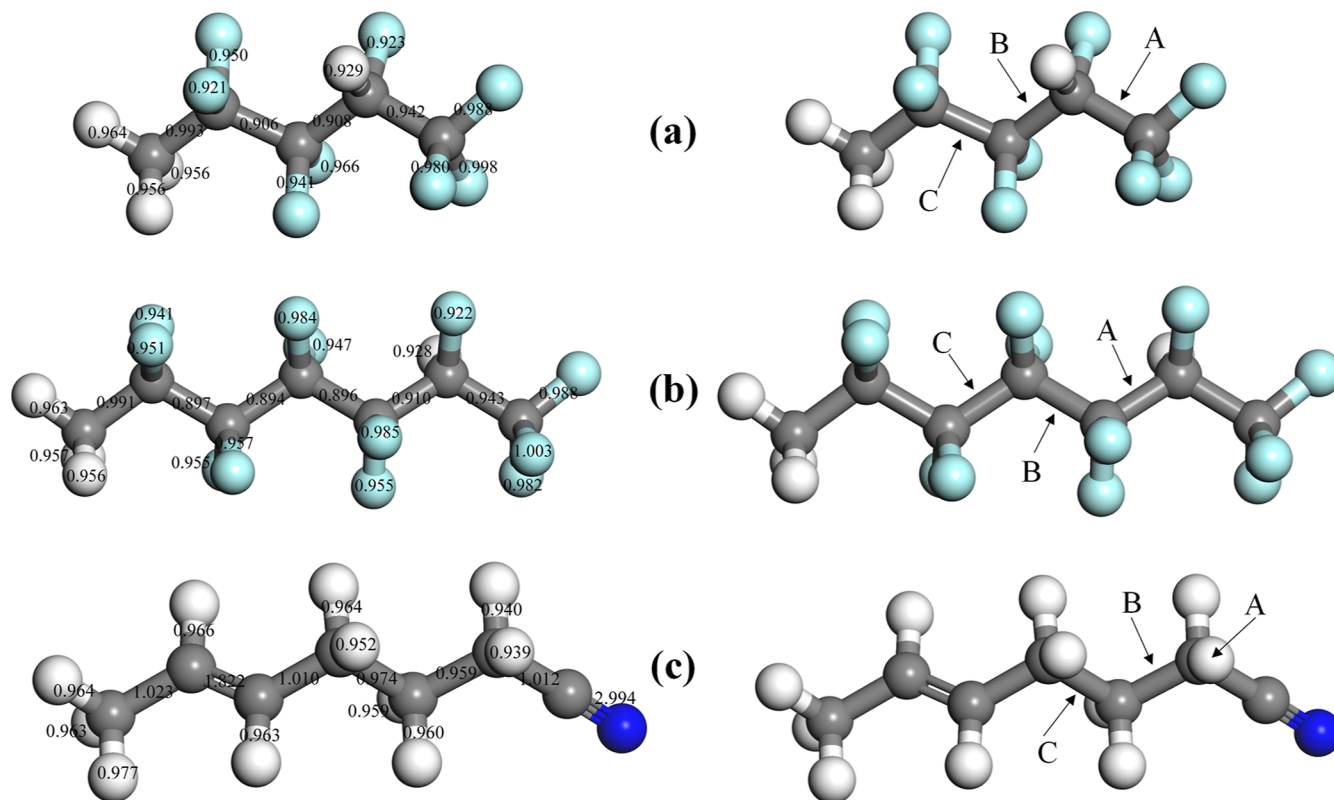


Figure 7. MBO and reaction paths of rubbers. (a) Type 26 FKM. (b) Type 246 FKM. (c) NBR.

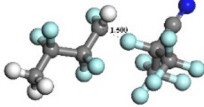
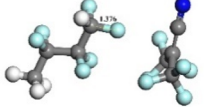
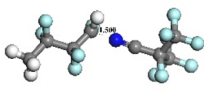
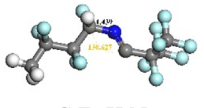
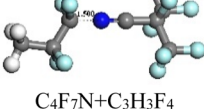
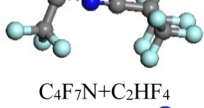
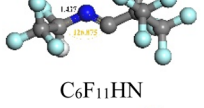
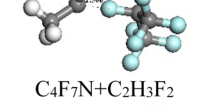
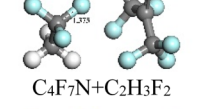
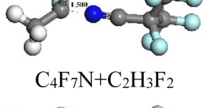
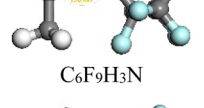
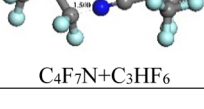
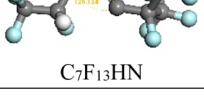
was used to perform gas component analysis. The mechanical behavior, morphology, and element composition of rubber samples were characterized by the universal testing machine Instron 5969, field emission scanning electron microscopy (FESEM), and X-ray photoelectron spectroscopy (XPS).

### 3. RESULTS AND DISCUSSION

**3.1. Morphology and Elemental Composition of Rubber after Interaction.** Figure 2 shows the rubber morphology after interaction in order to make each scanning

result more clearly reflect the relative content of each element; all the samples have been rescaled independently. The morphology of mixed FKM and NBR shows no obvious change in the  $C_4F_7N/CO_2$  and  $C_4F_7N/CO_2/O_2$  environment after the accelerated thermal aging tests at  $85\text{ }^\circ\text{C}$  for 28 days. As the temperature increased to  $100\text{ }^\circ\text{C}$ , white granular substances were produced on the FKM surface after interacting with  $C_4F_7N/CO_2$ , and agglomerated substances appeared for the  $C_4F_7N/CO_2/O_2$  environment. Thus, FKM is compatible with the  $C_4F_7N$  gas mixture at  $85\text{ }^\circ\text{C}$ , while a further increase

Table 1. Reaction between Type 26 FKM and C<sub>4</sub>F<sub>7</sub>N at 100 °C

Reaction	Reactant	Product	Enthalpy (kcal/mol)
A1	 C <sub>4</sub> F <sub>7</sub> N+C <sub>4</sub> H <sub>4</sub> F <sub>5</sub>	 C <sub>4</sub> F <sub>6</sub> N+C <sub>4</sub> H <sub>4</sub> F <sub>6</sub>	-22.188
A2	 C <sub>4</sub> F <sub>7</sub> N+C <sub>4</sub> H <sub>4</sub> F <sub>5</sub>	 C <sub>8</sub> F <sub>12</sub> H <sub>4</sub> N	-12.388
A3	 C <sub>4</sub> F <sub>7</sub> N+CF <sub>3</sub>	 C <sub>5</sub> F <sub>10</sub> N	-16.420
B1	 C <sub>4</sub> F <sub>7</sub> N+C <sub>3</sub> H <sub>3</sub> F <sub>4</sub>	 C <sub>7</sub> F <sub>11</sub> H <sub>3</sub> N	-19.297
B2	 C <sub>4</sub> F <sub>7</sub> N+C <sub>2</sub> HF <sub>4</sub>	 C <sub>6</sub> F <sub>11</sub> HN	-16.961
C1	 C <sub>4</sub> F <sub>7</sub> N+C <sub>2</sub> H <sub>3</sub> F <sub>2</sub>	 C <sub>4</sub> F <sub>7</sub> N+C <sub>2</sub> H <sub>3</sub> F <sub>2</sub>	-34.826
C2	 C <sub>4</sub> F <sub>7</sub> N+C <sub>2</sub> H <sub>3</sub> F <sub>2</sub>	 C <sub>6</sub> F <sub>9</sub> H <sub>3</sub> N	-14.060
C3	 C <sub>4</sub> F <sub>7</sub> N+C <sub>3</sub> HF <sub>6</sub>	 C <sub>7</sub> F <sub>13</sub> HN	-16.770

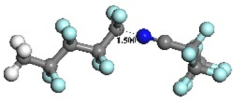
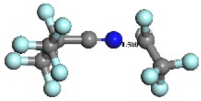
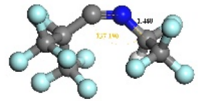
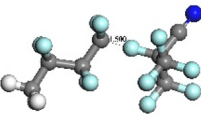
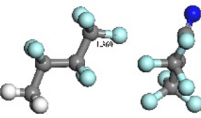
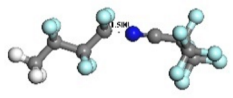
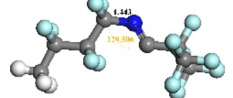
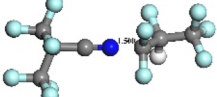
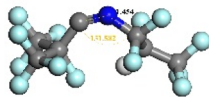
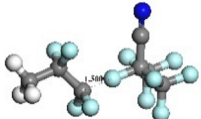
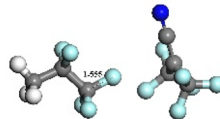
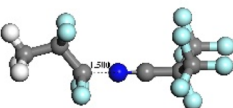
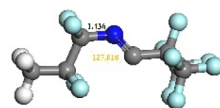
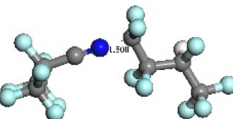
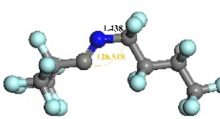
of temperature will lead to morphology change, and the presence of O<sub>2</sub> will exacerbate this process. As for NBR, the rubber surface that interacted with C<sub>4</sub>F<sub>7</sub>N/CO<sub>2</sub> at 100 °C generated uneven structures, and the multi-layer flake substance generated when interacted with C<sub>4</sub>F<sub>7</sub>N/CO<sub>2</sub>/O<sub>2</sub> indicated that O<sub>2</sub> would trigger the gas–solid interface.

Furthermore, we explored the element composition of the sample after tests. As shown in Figure 2k,l, C and F are derived from the rubber molecular chain, carbon black (C), and the C<sub>4</sub>F<sub>7</sub>N gas mixture.<sup>18</sup> The Zn, Mg, Ca, and Si originated from the reinforcing agents, such as zinc oxide (ZnO), magnesium oxide (MgO), calcium oxide (CaO), calcium sulfate (CaCO<sub>3</sub>), and silica white (SiO<sub>2</sub>).<sup>11,19</sup> The O element is derived from the reinforcing agent and peroxide cross-linker and its products, and S belongs to the vulcanizing agent introduced during the vulcanization process that forms sulfur–carbon cross-linking bonds in the rubber. No new element appeared on the FKM surface after the gas–solid interaction, while the content of Ca increased obviously at 100 °C, which indicated that the

interaction might cause the precipitation of reinforcing agents onto the surface to form the agglomerated block-like substances. XPS analysis was further conducted to investigate the element valency. As shown in Figure 3a, the C element is mainly in the form of C–C/C–H (284.8 eV), and the composition of CF<sub>3</sub> (293.6 eV), CF (291.2 eV), CF<sub>2</sub> (289.3 eV), and C–CF<sub>2</sub> (286.7 eV) also exists. The binding energy peaks of Ca and Mg located at 347.2, 350.7, and 1304 eV belong to the Ca 2p<sub>3/2</sub>, Ca 2p<sub>1/2</sub>, and Mg 1s, respectively. Overall, there were no new element valence states generated during the accelerated thermal aging tests.

As for the NBR, the interaction of C<sub>4</sub>F<sub>7</sub>N/CO<sub>2</sub> and C<sub>4</sub>F<sub>7</sub>N/CO<sub>2</sub>/O<sub>2</sub> at 85 °C did not cause obvious changes in element compositions (as shown in Figure 2l), indicating the chemical properties of NBR were maintained well. As the temperature reaches 100 °C, the F element appears on the NBR surface after interacting with C<sub>4</sub>F<sub>7</sub>N/CO<sub>2</sub> and C<sub>4</sub>F<sub>7</sub>N/CO<sub>2</sub>/O<sub>2</sub> (see the blue and purple lines in Figure 3l), inferring a strong chemical reaction occurred between them. The content of Mg,

Table 2. Reaction between Type 246 FKM and C<sub>4</sub>F<sub>7</sub>N at 100 °C

Reaction	Reactant	Product	Enthalpy (kcal/mol)
A1	 C <sub>4</sub> F <sub>7</sub> N + C <sub>5</sub> H <sub>3</sub> F <sub>8</sub>	 C <sub>9</sub> F <sub>15</sub> H <sub>3</sub> N	-16.026
A2	 C <sub>4</sub> F <sub>7</sub> N + C <sub>2</sub> HF <sub>4</sub>	 C <sub>6</sub> F <sub>11</sub> HN	-11.036
B1	 C <sub>4</sub> F <sub>7</sub> N + C <sub>4</sub> H <sub>3</sub> F <sub>6</sub>	 C <sub>4</sub> F <sub>6</sub> N + C <sub>4</sub> H <sub>3</sub> F <sub>7</sub>	-26.026
B2	 C <sub>4</sub> F <sub>7</sub> N + C <sub>4</sub> H <sub>3</sub> F <sub>6</sub>	 C <sub>8</sub> F <sub>13</sub> H <sub>3</sub> N	-12.448
B3	 C <sub>4</sub> F <sub>7</sub> N + C <sub>3</sub> HF <sub>6</sub>	 C <sub>7</sub> F <sub>13</sub> HN	-13.501
C1	 C <sub>4</sub> F <sub>7</sub> N + C <sub>3</sub> H <sub>3</sub> F <sub>4</sub>	 C <sub>4</sub> F <sub>6</sub> N + C <sub>3</sub> H <sub>3</sub> F <sub>5</sub>	-31.772
C2	 C <sub>4</sub> F <sub>7</sub> N + C <sub>3</sub> H <sub>3</sub> F <sub>4</sub>	 C <sub>7</sub> F <sub>11</sub> H <sub>3</sub> N	-19.175
C3	 C <sub>4</sub> F <sub>7</sub> N + C <sub>4</sub> HF <sub>8</sub>	 C <sub>8</sub> F <sub>15</sub> HN	-16.925

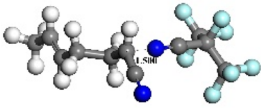
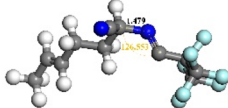
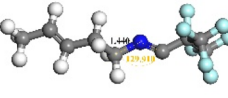
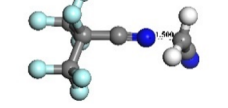
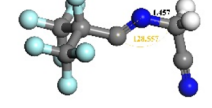
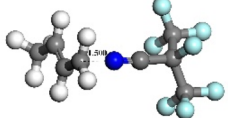
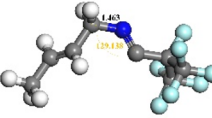
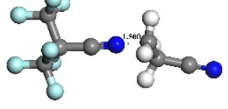
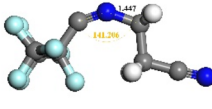
Si, and S elements also increased significantly, which was ascribed to the precipitation of the internal reinforcing agent and cross-linker crystals. The characteristic peak area of Ca increased with temperature (Figure 3b), which fits well with the microscopic morphology of multi-layer flake-like substances generated on the surface. In addition, the two characteristic peaks located at 684.5 and 688.3 eV corresponded to the C–F and –CF<sub>2</sub>CH<sub>2</sub>–, respectively, where C–F belongs to the inorganic fluorine component and –CF<sub>2</sub>CH<sub>2</sub>– belongs to the –CF<sub>x</sub>CH<sub>x</sub>– group, corresponding to the organic fluorine component.<sup>10</sup> The peak area of C–F and –CF<sub>2</sub>CH<sub>2</sub>– increased significantly with temperature, indicating that the reaction between the C<sub>4</sub>F<sub>7</sub>N gas mixture and NBR leads to the accumulation of the F element. Overall, the compatibility between the C<sub>4</sub>F<sub>7</sub>N gas mixture and

NBR is poor at 100 °C. The increase of temperature or the addition of O<sub>2</sub> will intensify the gas–solid interaction.

**3.2. Mechanical Properties of Rubber after Interaction.** Compressive mechanical properties are important indicators that reflect the sealing performance of rubber sealing rings, which is also of great significance for the safe operation of GIE. To further analyze the influence of the gas–solid interaction on the mechanical properties of sealing rubber, the mechanical properties of the rubber samples were tested, including the compressive modulus and the permanent compression deformation.

As shown in Figure 4, the initial compressive moduli of FKM and NBR are 5.285 and 5.292 MPa, respectively. The compressive modulus of NBR increased slightly after interacting with C<sub>4</sub>F<sub>7</sub>N/CO<sub>2</sub>/O<sub>2</sub> at 85 °C. As the temperature reaches 100 °C, its value decreases by 22.81 and 6.84% after

Table 3. Reaction between NBR and C<sub>4</sub>F<sub>7</sub>N at 100 °C

Reaction	Reactant	Product	Enthalpy (kcal/mol)
A	 C <sub>4</sub> F <sub>7</sub> N + C <sub>7</sub> F <sub>10</sub> N	 C <sub>11</sub> F <sub>17</sub> N <sub>2</sub>	-4.108
B1	 C <sub>4</sub> F <sub>7</sub> N + C <sub>5</sub> H <sub>9</sub>	 C <sub>9</sub> F <sub>7</sub> H <sub>9</sub> N	-18.745
B2	 C <sub>4</sub> F <sub>7</sub> N + C <sub>2</sub> H <sub>2</sub> N	 C <sub>6</sub> F <sub>7</sub> H <sub>2</sub> N <sub>2</sub>	-5.211
C1	 C <sub>4</sub> F <sub>7</sub> N + C <sub>4</sub> H <sub>7</sub>	 C <sub>8</sub> F <sub>7</sub> H <sub>7</sub> N	-4.592
C2	 C <sub>4</sub> F <sub>7</sub> N + C <sub>3</sub> H <sub>4</sub> N	 C <sub>7</sub> F <sub>7</sub> H <sub>4</sub> N <sub>2</sub>	-17.425

interacting with C<sub>4</sub>F<sub>7</sub>N/CO<sub>2</sub> and C<sub>4</sub>F<sub>7</sub>N/CO<sub>2</sub>/O<sub>2</sub> gas mixtures. The addition of O<sub>2</sub> could significantly inhibit the decrease of the compressive modulus. It is reported that the aging of rubber under thermal oxygen conditions is usually dominated by O<sub>2</sub>, and the oxidation mechanism will lead to the cross-linking and cracking reactions of molecular chains at the same time.<sup>20</sup> Generally, the cross-linking reactions increase the density and hardness of rubber, while the cracking reactions work on the contrary, and the final strength of the rubber depends on the rate at which the two proceed.<sup>21</sup> In addition, the ends of broken molecular chains may oxidize to form polar groups that enhance intermolecular attractiveness, and plasticizer loss can also lead to increased hardness of rubber.<sup>22,23</sup> Accordingly, multiple factors such as cross-linking, cracking, oxidation reaction, and plasticizer loss could have influences on the compressive mechanical properties. Phthalates are the majority of plasticizers, accounting for more than 80% of the market share of plasticizers. The molecular structure of phthalate contains a carbon–carbon double bond, a carbon–oxygen double bond, and a carbon–oxygen bond.<sup>24</sup> However, it can be seen from Figure 3a that the characteristic peaks of the above three molecular bonds do not appear, indicating there was no obvious plasticizer precipitation on the FKM surface, which indicated that there was almost no loss of plasticizer during the experiment. Therefore, it is speculated that the cross-linking reaction is dominant and the rubber cross-linking density increases, resulting in an

increase in the compressive modulus of elasticity. Under the same experimental conditions, the molecular structure of FKM is compact to maintain the mechanical strength, while NBR has obvious structural damage at 100 °C, resulting in a significant deterioration of compressive mechanical properties.

Besides, the permanent compression deformation of FKM increased by 6.75 and 7.26% after interacting with C<sub>4</sub>F<sub>7</sub>N/CO<sub>2</sub> and C<sub>4</sub>F<sub>7</sub>N/CO<sub>2</sub>/O<sub>2</sub> as the temperature changed from 85 to 100 °C, respectively, which is lower than that of NBR (8.16 and 14.66%), indicating that a higher temperature will weaken the compression recovery performance of rubber. The addition of O<sub>2</sub> resulted in the increase of the compressive modulus and permanent compression deformation. This is ascribed to the excessive cross-linking density that causes dense internal cross-linking molecular chains and lower uniformity. The stress concentration area is more likely to produce molecular chain fractures and cause collapse. Thus, the rubber's self-recovery performance is weakened.<sup>21</sup> In addition, it is reported that the internal chemical reaction rate in rubber is suppressed by diffusion-limited oxidation (DLO), which helps maintain the elasticity and recovery performance.<sup>25,26</sup> The DLO effect occurs when oxygen diffusion into the material cannot keep up with oxygen consumption due to aging. Because of the consequential shortage of oxygen in the interior sample, it can be seen from Figure 4 that the effect of oxygen on the mechanical properties of NBR is significantly greater than that of FKM, and it is presumed that oxygen has greater

permeability in NBR, the DLO effect is weaker in the NBR experimental group, and the aging degree of NBR is higher.

Overall, the mechanical performance of FKM is superior to that of NBR. The long-term gas–solid interaction will cause inferior mechanical property deterioration, which demonstrates better sealing performance and a safer, more reliable application potential.

### 3.3. Analysis of Gas Components after Interaction.

The gas composition after interaction was also considered to evaluate the compatibility, and the gas chromatogram under different conditions is given in Figure 5.

It can be found that the interaction of the  $C_4F_7N$  gas mixture and FKM and NBR will produce gas decomposition products including carbon monoxide (CO), hexafluoropropylene ( $C_3F_6$ ), and trifluoroacetonitrile ( $CF_3CN$ ). CO is generated by the reaction between  $O_2$  and carbon black (C) or the decomposition of the additive substance, considering the decomposition or reduction of  $CO_2$  requires a high temperature of 1000 °C–2300 °C. The CO content in the ternary gas experimental group was significantly higher than that of the binary gas because of the adequate  $O_2$ . In addition, some studies<sup>20,27</sup> report that  $O_2$  usually leads to the oxidation of rubber molecular side chains, generating ketones, aldehydes, acids, peroxides, alcohols, and gaseous decomposition products such as CO and  $CO_2$  during the thermal aging process. The content of  $C_3F_6$  and  $CF_3CN$  in the FKM group was significantly higher than that in the NBR group.  $C_3F_6$  mainly comes from the decomposition of  $C_4F_7N$ , and  $CF_3CN$  mainly comes from the combination of  $CF_3$  and CN.<sup>28</sup> The content of these two gases is also higher in the  $C_4F_7N/CO_2/O_2$  experimental group.

It should be noted that the experimental temperature is much lower than the initial thermal decomposition temperature of  $C_4F_7N$  (350 °C).<sup>29</sup> Thus, the gas–solid rubber undergoes reactions with moderate conditions to produce  $C_3F_6$  and  $CF_3CN$ . In addition, it is reported that nitrile substances will decompose under alkaline conditions.<sup>30</sup> Considering MgO and CaO are alkaline oxides and  $CaCO_3$  is a strong base-weak acid salt, which may also lead to the decomposition of  $C_4F_7N$ .<sup>11</sup> Moreover, the FKM molecular chains are rich in  $CF_3$ , F, and other fluorine-containing groups, and the NBR molecular chains also contain CN groups. The combination of free radicals produced by the cracking of rubber chains and the decomposition of  $C_4F_7N$  in thermal acceleration experiments also promoted the generation of  $C_3F_6$  and  $CF_3CN$ . As NBR does not contain the F element, the fluorine-containing radicals only have a source of  $C_4F_7N$ . Thus, the content of  $C_3F_6$  and  $CF_3CN$  after interacting with NBR is significantly lower than that of FKM. It is noteworthy that the addition of  $O_2$  also promotes the formation of three main gas components.

**3.4. Gas–Solid Interaction Mechanism.** Considering the aging temperature set in this work is much lower than the initial thermal decomposition of  $C_4F_7N$ , the generation of gas by-products as well as the morphological change of rubber are ascribed to the gas–solid chemical reactions. As illustrated in Figure 6, some specific molecular bonds of rubber will break under heating conditions,  $C_4F_7N$  and these newly formed unsaturated groups are more likely to have chemical reactions compared to the simple decomposition of  $C_4F_7N$ . Besides, there originally exist unsaturated components on the rubber surface, which will also interact with  $C_4F_7N$  to generate by-products. We further calculated the reaction enthalpy between  $C_4F_7N$  and rubber monomer molecules based on DFT to

understand the gas–solid interaction mechanism. DFT calculations were conducted using the Dmol3 package of Materials Studio. The generalized gradient approximation with the Perdew–Burke–Ernzerhof exchange–correlation function was used for geometric optimization.<sup>31,32</sup> The double numerical polarization was selected as the atomic orbital basis set, and the density functional semi-core pseudopotential (DSPP) was applied considering the relativistic effect of transition.<sup>33,34</sup> The direct inversion in the iterative subspace was used to speed up the convergence rate of the self-consistent field electron density.<sup>35</sup> The convergence criteria for geometric optimization were set with  $1 \times 10^{-5}$  Ha for energy, 0.002 Ha/Å for the maximum force, and 0.005 Å for maximum displacement.<sup>33,36</sup>

The reaction enthalpy ( $E_a$ ) is defined as follows<sup>37</sup>

$$E_{\text{enthalpy}} = E_{\text{product}} - E_{\text{reactant}} \quad (1)$$

Figure 7 shows the optimized structure of type 26, type 246 FKM, and NBR monomer molecules and the corresponding Mayer bond order (MBO), respectively.<sup>38</sup> The bond strength of  $C \equiv N$  and  $C = C$  is the highest, with the MBO reaching 2.994 and 1.822, respectively. Herein, we mainly considered three bond cleavage paths of FKM and NBR, as shown in Figure 7. Table 1 shows the reaction paths and enthalpy between the decomposition groups of type 26 FKM and  $C_4F_7N$ . The F atoms linked to the central C atoms of  $C_4F_7N$  detach from the  $C_4F_7N$  molecule and form new bonds with the unsaturated C in  $C_4H_4F_5$  and  $C_2H_3F_2$  to generate  $C_4H_4F_6$  (−22.188 kcal/mol) and  $C_2H_3F_3$  (−34.826 kcal/mol) through paths A1 and C1, respectively. These two paths have the highest reaction enthalpy, which makes them more likely to occur. For other reaction paths, the gas–solid interaction causes the formation of  $C \equiv N$  in between  $C_4F_7N$  and the rubber monomer.

As for the type 246 FKM, the F atoms linked to the central C atoms of  $C_4F_7N$  detach and form new bonds with the unsaturated C in  $C_4H_3F_6$  and  $C_3H_3F_4$  to generate  $C_4H_3F_7$  and  $C_3H_3F_5$  through paths B1 and C1 and also demonstrated the largest enthalpy of −26.026 and −31.772 kcal/mol, respectively (Table 2). The other paths result in the generation of  $C_9F_{13}H_3N$ ,  $C_6F_{11}HN$ ,  $C_8F_{13}H_3N$ ,  $C_7F_{13}HN$ ,  $C_7F_{11}H_3N$ , and  $C_8F_{13}HN$ , all of which have lower enthalpy. Combined with the results obtained in Table 1, the accumulation of the F element mainly occurred through the detachment of central F in  $C_4F_7N$  to form a new bond with the unsaturated C atom in rubber monomers.

Table 3 shows the reaction paths and enthalpy changes between the decomposition groups of NBR and  $C_4F_7N$ . Bond binding of N in  $C_4F_7N$  and unsaturated C atoms in rubber monomers will occur, and the reaction enthalpies through paths B1 (−18.745 kcal/mol) and C2 (−17.425 kcal/mol) are the highest with the bond length shortened to 1.440 and 1.447 Å. Therefore, the accumulation of the F element on the surface of NBR mainly comes from the adsorption of  $C_4F_7N$ .

Overall, the adsorption of  $C_4F_7N$  and the bonding of central F with rubber monomers can both result in the accumulation of fluorine. Accordingly, the FKM surface has both the adsorbed  $C_4F_7N$  and bonded C–F, while NBR is mainly composed of the adsorbed  $C_4F_7N$ . Combined with the morphology and mechanical property test results, the adsorption of  $C_4F_7N$  is more likely to cause damage to the microstructure of rubber and the deterioration of mechanical properties. As the temperature increases, the cracking rate of

NBR is accelerated and the surface-adsorbed  $C_4F_7N$  will move intensely or even diffuse to the interior of rubber, further causing the reaction of unsaturated structure or additives and exacerbating the internal structure destruction, macroscopically bringing significant morphology and mechanical property deterioration. On the whole, FKM has the potential to be used as the sealing material for  $C_4F_7N$  gas mixture-based GIE.

#### 4. CONCLUSIONS

Herein, we investigated the compatibility of the  $C_4F_7N$  gas mixture with FKM and NBR to reveal the effect of the gas–solid interface interaction on rubber morphology, mechanical properties, and gas compositions. The interaction mechanism of gas–solid rubber was further analyzed. The following conclusions can be obtained.

- (1) FKM and NBR are relatively stable under  $C_4F_7N/CO_2$  and  $C_4F_7N/CO_2/O_2$  environments at 85 °C. At 100 °C, the interaction between  $C_4F_7N$  and rubber causes microscopic structural damage and the precipitation of the crystals of the vulcanizing agent and the reinforcing agent. The addition of  $O_2$  further promotes the cracking reactions. The adsorption of  $C_4F_7N$  molecules on the rubber surface or the reaction between them caused the accumulation of the F element, and the gas by-products  $CO$ ,  $C_3F_6$ , and  $CF_3CN$  were generated.
- (2) The interaction between the  $C_4F_7N$  gas mixture and FKM will not lead to the deterioration of mechanical properties. The compressive modulus increased, and the permanent compression deformation is within 25%. The mechanical properties of NBR significantly deteriorated after the interaction, with a decrease of the compressive modulus and a weakening of the self-recovery performance.
- (3) The reaction between  $C_4F_7N$  and the unsaturated groups on the rubber surface is dominated by the transfer of the central F atom in  $C_4F_7N$  and the bonding of the N atom with the unsaturated C atom. The main F element accumulation paths on the FKM and NBR are the chemical reaction of the F atom and the adsorption of the  $C_4F_7N$  molecule, respectively.
- (4) The compatibility between FKM and the  $C_4F_7N$  gas mixture is superior to that of NBR, which demonstrates application potential as a sealing material for  $C_4F_7N$  gas mixture-based GIE.

#### ■ AUTHOR INFORMATION

##### Corresponding Authors

**Mingli Fu** – Electric Power Research Institute, China Southern Power Grid, Guangzhou 510623, China; National Engineering Research Center of UHV Technology and New Electrical Equipment Fundamentals, Guangzhou 510623, China; United Laboratory of Advanced Electrical Materials and Equipment Support Technology, China Southern Power Grid, Guangzhou 510623, China; Email: [fumli@csg.cn](mailto:fumli@csg.cn)

**Xiangyu Tan** – Power Science Research Institute of Yunnan Power Grid Co., Ltd, Kunming 650217, China; Email: [89579253@qq.com](mailto:89579253@qq.com)

##### Authors

**Ran Zhuo** – Electric Power Research Institute, China Southern Power Grid, Guangzhou 510623, China; National Engineering Research Center of UHV Technology and New

Electrical Equipment Fundamentals, Guangzhou 510623, China; United Laboratory of Advanced Electrical Materials and Equipment Support Technology, China Southern Power Grid, Guangzhou 510623, China

**Junyi Chen** – School of Electrical Engineering and Automation, Wuhan University, Wuhan 430072, China; [orcid.org/0000-0002-4199-8781](https://orcid.org/0000-0002-4199-8781)

**Song Xiao** – School of Electrical Engineering and Automation, Wuhan University, Wuhan 430072, China

**Dibo Wang** – Electric Power Research Institute, China Southern Power Grid, Guangzhou 510623, China; National Engineering Research Center of UHV Technology and New Electrical Equipment Fundamentals, Guangzhou 510623, China; United Laboratory of Advanced Electrical Materials and Equipment Support Technology, China Southern Power Grid, Guangzhou 510623, China; [orcid.org/0000-0002-1105-6339](https://orcid.org/0000-0002-1105-6339)

**Yi Li** – School of Electrical Engineering and Automation, Wuhan University, Wuhan 430072, China

**Peng Wu** – School of Electrical Engineering and Automation, Wuhan University, Wuhan 430072, China; [orcid.org/0000-0001-8578-5051](https://orcid.org/0000-0001-8578-5051)

**Ju Tang** – School of Electrical Engineering and Automation, Wuhan University, Wuhan 430072, China

**Xiaoxing Zhang** – Key Laboratory for High-efficiency Utilization of Solar Energy and Operation Control of Energy Storage System, School of Electrical and Electronic Engineering, Hubei University of Technology, Wuhan 430068, China; [orcid.org/0000-0001-5872-2039](https://orcid.org/0000-0001-5872-2039)

Complete contact information is available at:

<https://pubs.acs.org/10.1021/acsomega.3c00195>

#### Notes

The authors declare no competing financial interest.

#### ■ ACKNOWLEDGMENTS

This work was supported by the science and technology project of the China Southern Power Grid (Grant numbers YNKJXM20222118, YNKJXM20222131, and YNKJXM20222043).

#### ■ REFERENCES

- (1) Rabie, M.; Franck, C. M. Assessment of eco-friendly gases for electrical insulation to replace the most potent industrial greenhouse gas  $SF_6$ . *Environ. Sci. Technol.* **2018**, *52*, 369–380.
- (2) Zhang, X.; Yu, L.; Wu, X.; Hu, W. Experimental sensing and density functional theory study of  $H_2S$  and  $SO_2$  adsorption on Au-modified graphene. *Adv. Sci.* **2015**, *2*, 1500101.
- (3) Cui, H.; Zhang, X.; Zhang, J.; Zhang, Y. Nanomaterials-based gas sensors of  $SF_6$  decomposed species for evaluating the operation status of high-voltage insulation devices. *High Volt.* **2019**, *4*, 242–258.
- (4) Kieffel, Y.; Irwin, T.; Ponchon, P.; Owens, J. Green gas to replace  $SF_6$  in electrical grids. *IEEE Power Energy Mag.* **2016**, *14*, 32–39.
- (5) Lindner, C.; Gautsch, D. Application of a fluoronitrile gas in a 123 kV GIS pilot substation. *CIGRE reports* **2018**, B3–B146.
- (6) Gao, C.; Zhang, Z.; Hao, Y.; Yang, L.; Peng, J.; Wang, G.; Yang, Y.; Li, L. A Review on Test Methods and Lifetime Prediction of GIS Seal Rings. In *Conference on Power System Technology (POWERCON)*. IEEE, 2018; pp 3891–3902. DOI: [10.1109/powercon.2018.8601582](https://doi.org/10.1109/powercon.2018.8601582)
- (7) Montanari, G. C. Bringing an Insulation to Failure: the Role of Space Charge. *IEEE Trans. Dielectr. Electr. Insul.* **2011**, *18*, 339–364.
- (8) Gorur, R. S.; Cherney, E. A.; Hackam, R. The AC and DC performance of polymeric insulating materials under accelerated aging in a fog chamber. *IEEE Trans. Power Deliv.* **1998**, *3*, 1892–1920.

- (9) Kessler, F.; Sarfert-Gast, W.; Ise, M.; Goll, F. Interaction of low global warming potential gaseous dielectrics with materials of gas-insulated systems. *Proceedings 20th International Symposium High Voltage Engineering*, 2017;.
- (10) Li, Y.; Zhang, X.; Li, Y.; Chen, D.; Cui, Z.; Liu, W.; Tang, J. Interaction mechanism between the C<sub>4</sub>F<sub>7</sub>N–CO<sub>2</sub> gas mixture and the EPDM seal ring. *ACS Omega* **2020**, *5*, 5911–5920.
- (11) Zheng, Z.; Li, H.; Zhou, W.; Yu, J.; Wang, H.; Zhang, J.; Jiang, Y.; Zhao, J.; Yang, L.; Zhou, Y. Compatibility between C<sub>4</sub>F<sub>7</sub>N and the sealing material EPDM used in GIL. *2019 IEEE Conference on Electrical Insulation and Dielectric Phenomena (CEIDP)*, 2019; pp 146–149.
- (12) Ferrandez, P. Fluoroelastomers, FKM, and FEPM. In *Handbook of Specialty Elastomers*, 1st ed.; Robert, C. K., Ed.; Taylor & Francis Group: New York, 2008, pp 133–154.
- (13) Liu, J.; Li, X.; Xu, L.; Zhang, P. Investigation of aging behavior and mechanism of nitrile-butadiene rubber (NBR) in the accelerated thermal aging environment. *Polym. Test.* **2016**, *54*, 59–66.
- (14) Améduri, B.; Boutevin, B.; Kostov, G. Fluoroelastomers: synthesis, properties and applications. *Prog. Polym. Sci.* **2001**, *26*, 105–187.
- (15) Zhang, X.; Chen, Q.; Zhang, J.; Li, Y.; Xiao, S.; Zhou, R.; Tang, J. Experimental study on power frequency breakdown characteristics of C<sub>4</sub>F<sub>7</sub>N/CO<sub>2</sub> gas mixture under Quasi-Homogeneous electric field. *IEEE Access* **2018**, *7*, 19100–19108.
- (16) Ambo, N. F.; Zainuddin, H.; Kamarudin, M. S.; Wari, J. M.; Zahari, A. The effect of pressure and gap distance to AC breakdown behavior of SF<sub>6</sub>/N<sub>2</sub> gas mixtures. *2018 2nd International Conference on Electrical Engineering and Informatics (Icon EEI). IEEE*, 2018; pp 144–147.
- (17) Li, Y.; Zhang, X.; Ye, F.; Chen, D.; Tian, S.; Cui, Z. Influence regularity of O<sub>2</sub> on dielectric and decomposition properties of C<sub>4</sub>F<sub>7</sub>N–CO<sub>2</sub>–O<sub>2</sub> gas mixture for medium-voltage equipment. *High Volt.* **2020**, *5*, 256–263.
- (18) Xu, Z.; Zhang, Y.; Li, A.; Wang, J.; Wang, G.; He, Q. Research progress on compounding agent and mechanical test method of fluororubber. *J. Appl. Polym. Sci.* **2021**, *138*, 50913.
- (19) Radosavljević, J.; Nikolić, L.; Nikolić, M.; Ilić-Stojanović, S. Effect of ZnO on mechanical and electrical properties of peroxide cured EPDM. *Int. Polym. Process.* **2018**, *33*, 695–705.
- (20) Gillen, K. T.; Celina, M.; Clough, R. L. Density measurements as a condition monitoring approach for following the aging of nuclear power plant cable materials. *Radiat. Phys. Chem.* **1999**, *56*, 429–447.
- (21) Zhao, J.; Yang, R.; Iervolino, R.; Barbera, S. Investigation of crosslinking in the thermooxidative aging of nitrile–butadiene rubber. *J. Appl. Polym. Sci.* **2015**, *132*, 41319.
- (22) Kömmling, A.; Jaunich, M.; Goral, M.; Wolff, D. Insights for lifetime predictions of O-ring seals from five-year long-term aging tests. *Polym. Degrad. Stab.* **2020**, *179*, 109278.
- (23) Liu, X.; Zhao, J.; Liu, J.; Yang, R. Volatile components changes during thermal aging of nitrile rubber by flash evaporation of Py-GC/MS. *J. Anal. Appl. Pyrolysis* **2015**, *113*, 193–201.
- (24) Da Silva, M. A.; Vieira, M. G. A.; Maçumoto, A. C. G.; Beppu, M. M. Polyvinylchloride (PVC) and natural rubber films plasticized with a natural polymeric plasticizer obtained through polyesterification of rice fatty acid. *Polym. Test.* **2011**, *30*, 478–484.
- (25) Kömmling, A.; Jaunich, M.; Wolff, D. Effects of heterogeneous aging in compressed HNBR and EPDM O-ring seals. *Polym. Degrad. Stab.* **2016**, *126*, 39–46.
- (26) Kömmling, A.; Jaunich, M.; Pourmand, P.; Wolff, D.; Gedde, U. W. Influence of ageing on sealability of elastomeric O-rings. *Macromol. Symp.* **2017**, *373*, 1600157.
- (27) Gillen, K. T.; Bernstein, R.; Wilson, M. H. Predicting and confirming the lifetime of o-rings. *Polym. Degrad. Stab.* **2005**, *87*, 257–270.
- (28) Ye, F.; Zhang, X.; Xie, C.; Sun, X.; Wu, P.; Xiao, S.; Tang, J.; Li, Y. Effect of oxygen and temperature on thermal decomposition characteristics of C<sub>4</sub>F<sub>7</sub>N/CO<sub>2</sub>/O<sub>2</sub> gas mixture for MV equipment. *IEEE Access* **2020**, *8*, 221004–221012.
- (29) Zhang, X.; Zhang, Y.; Huang, Y.; Li, Y.; Cheng, H.; Xiao, S. Detection of decomposition products of C<sub>4</sub>F<sub>7</sub>N–CO<sub>2</sub> gas mixture based on infrared spectroscopy. *Vib. Spectrosc.* **2020**, *110*, 103114.
- (30) *Basic organic chemistry*, 4th ed.; Xing, Q.; Pei, W.; Xu, R., Eds.; Peking University Press: Beijing, 2016; pp 543–544.
- (31) Grimme, S. Semiempirical GGA-type density functional constructed with a long-range dispersion correction. *J. Comput. Chem.* **2006**, *27*, 1787–1799.
- (32) Matveev, A.; Stauffer, M.; Mayer, M.; Rösch, N. Density functional study of small molecules and transition-metal carbonyls using revised PBE functionals. *Int. J. Quantum Chem.* **1999**, *75*, 863–873.
- (33) Delley, B. An all-electron numerical method for solving the local density functional for polyatomic molecules. *J. Chem. Phys.* **1990**, *92*, 508–517.
- (34) Malik, P.; Thareja, R.; Singh, J.; Kakkar, R. II–VI core/shell quantum dots and doping with transition metal ions as a means of tuning the magnetoelectronic properties of CdS/ZnS core/shell QDs: A DFT study. *J. Mol. Graphics Modell.* **2022**, *111*, 108099.
- (35) Maschio, L. Direct inversion of the iterative subspace (DIIS) convergence accelerator for crystalline solids employing Gaussian basis sets. *Theor. Chem. Acc.* **2018**, *137*, 60.
- (36) Cui, H.; Zhang, X.; Zhang, J.; Tang, J. Adsorption behaviour of SF<sub>6</sub> decomposed species onto Pd<sub>4</sub>-decorated single-walled CNT: a DFT study. *Mol. Phys.* **2018**, *116*, 1749–1755.
- (37) Boys, S. F.; Bernardi, F. The calculation of small molecular interactions by the differences of separate total energies. Some procedures with reduced errors. *Mol. Phys.* **1970**, *19*, 553–566.
- (38) Wu, H.; Xia, Y.; Zhang, C.; Xie, S.; Wu, S.; Cui, H. Adsorptions of C<sub>5</sub>F<sub>10</sub>O decomposed compounds on the Cu-decorated NiS<sub>2</sub> monolayer: a first-principles theory. *Mol. Phys.* **2023**, e2163715.